Earthquake Engineering & Structural Dynamics
The Journal of the International Association for Earthquake Engineering

EARTHQUAKE ENGINEERING & STRUCTURAL DYNAMICS
*Earthquake Engng Struct. Dyn.* 2016
Published online in Wiley Online Library (wileyonlinelibrary.com). DOI: 10.1002/eqe.2856

# Experimental study of deformable connection consisting of buckling-restrained brace and rubber bearings to connect floor system to lateral force resisting system

Georgios Tsampras[1,*,†], Richard Sause[2], Robert B. Fleischman[3] and Jose I. Restrepo[4]

[1]*Simpson Gumpertz & Heger Inc., Waltham, MA, USA*
[2]*Lehigh University, Bethlehem, PA, USA*
[3]*Department of Civil Engineering and Engineering Mechanics, University of Arizona, Tucson, AZ, USA*
[4]*Department of Structural Engineering, University of California, San Diego, CA, USA*

## SUMMARY

This paper presents experimental and numerical studies of a full-scale deformable connection used to connect the floor system of the flexible gravity load resisting system to the stiff lateral force resisting system (LFRS) of an earthquake-resistant building. The purpose of the deformable connection is to limit the earthquake-induced horizontal inertia force transferred from the floor system to the LFRS and, thereby, to reduce the horizontal floor accelerations and the forces in the LFRS. The deformable connection that was studied consists of a buckling-restrained brace (BRB) and steel-reinforced laminated low-damping rubber bearings (RB).

The test results show that the force–deformation responses of the connection are stable, and the dynamic force responses are larger than the quasi-static force responses. The BRB+RB force–deformation response depends mainly on the BRB response. A detailed discussion of the BRB experimental force–deformation response is presented. The experimental results show that the maximum plastic deformation range controls the isotropic hardening of the BRB. The hardened BRB force–deformation responses are used to calculate the overstrength adjustment factors. Details and limitations of a validated, accurate model for the connection force–deformation response are presented. Numerical simulation results for a 12-story reinforced concrete wall building with deformable connections show the effects of including the RB in the deformable connection and the effect of modeling the BRB isotropic hardening on the building seismic response. Copyright © 2016 John Wiley & Sons, Ltd.

Received 5 July 2016; Revised 14 November 2016; Accepted 14 November 2016

KEY WORDS: deformable connection; full-scale experimental validation; dynamic testing; buckling-restrained brace; low-damping rubber bearings

## 1. INTRODUCTION

The development of a deformable connection used to connect the floor system of a flexible gravity load resisting system (GLRS) to the stiff lateral force resisting system (LFRS) of a building designed to resist earthquake loading was presented in [1]. In comparison with a conventional earthquake-resistant building, the use of a well-designed deformable connection at each floor in the building was shown to limit the earthquake-induced horizontal inertia forces transferred from the floor to the LFRS and reduce the floor accelerations, without significantly increasing the lateral drift [1]. The use of deformable connections also significantly reduces the dispersion in the peak forces transferred from the floor systems to the LFRS, in the peak floor accelerations, and in the peak LFRS story

*Correspondence to: Georgios Tsampras, Staff II, Simpson Gumpertz & Heger Inc., Waltham, MA, USA.
†E-mail: tsampras.g@gmail.com

Copyright © 2016 John Wiley & Sons, Ltd.

shears [1]. Thus, a more reliable building system design is possible by reducing the variability in the lateral force and acceleration responses, given the expected earthquake ground motion variability [1].

The deformable connection described in [1] consists of a limited-strength hysteretic component and low-damping rubber bearings. The limited-strength hysteretic component transfers lateral force from the floor system to the LFRS and maintains the stability of the GLRS. The low-damping laminated rubber bearings maintain the out-of-plane stability of the LFRS and provide additional post-elastic stiffness to the deformable connection.

This paper presents experimental and numerical studies of a full-scale deformable connection that uses a buckling-restrained brace (BRB) as the limited-strength hysteretic component and a set of four steel-reinforced laminated low-damping rubber bearings (RB). The deformable connection that was studied is denoted as BRB+RB. Two BRB+RB connection specimens were tested, denoted as BRB#1+RB and BRB#2+RB, respectively. The two specimens had different BRBs with the same BRB design and used the same set of four RB. Each BRB+RB specimen was subjected to quasi-static earthquake and sinusoidal deformation histories and to dynamic sinusoidal deformation histories.

The present paper provides new information about the BRB+RB deformable connection, compared with [1], as follows: (1) This paper presents detailed experimental results from tests on two BRB+RB connection specimens, including (a) a presentation of experimental response under various types of loading, (b) a study of the hardening behavior of BRBs under symmetric and unsymmetric deformation histories showing the relationship of this hardening to different deformation parameters, and (c) the hardened BRB force–deformation responses are used to calculate the overstrength adjustment factors; (2) this paper presents the details and limitations of a validated, accurate model for the force–deformation response of the BRB+RB connection; and (3) this paper includes numerical simulation results for a 12-story reinforced concrete wall building with deformable connections to show the effects of including the RB in the deformable connection and the effects of modeling the BRB isotropic hardening on the building seismic response.

## 2. EXPERIMENTAL SETUP

Figure 1 shows the experimental setup used to test the BRB+RB connection specimens. A simulated floor system and a reinforced concrete shear wall LFRS were built in the laboratory. The south end of the BRB was attached to the LFRS, and the north end of the BRB was attached to a built-up steel beam that was part of the simulated floor system. Clevis connections with spherical bearings at each end of the BRB were used to attach the BRB to the LFRS and the floor system. Each BRB+RB

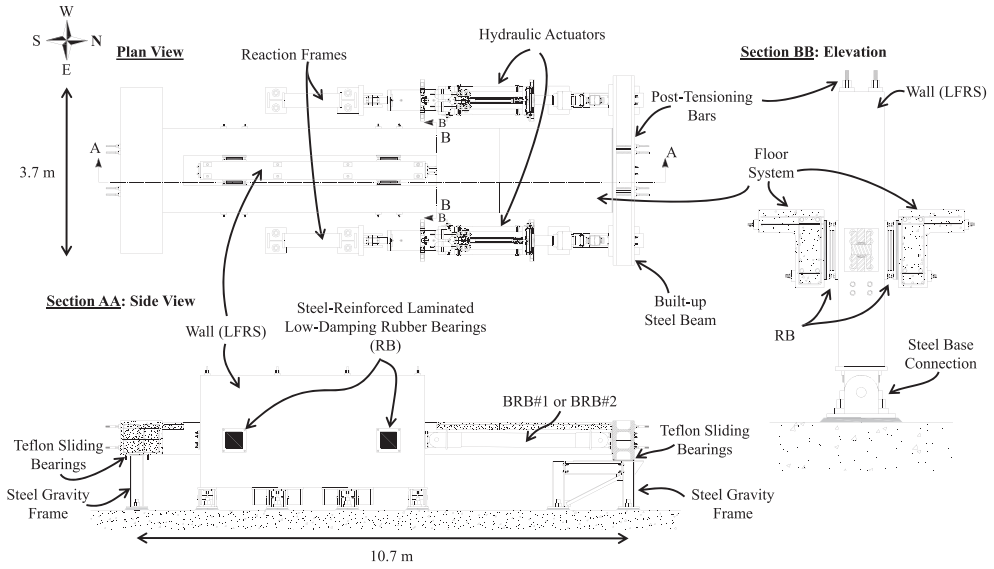



Figure 1. Plan view, section AA, and section BB of experimental setup.

Copyright © 2016 John Wiley & Sons, Ltd.

DOI: 10.1002/eqe

connection specimen was deformed by subjecting the floor system to predefined displacement (relative to the lab strong floor) histories in the north–south (NS) direction, by using hydraulic actuators [2] that were supported by a steel reaction frame at the south end and the built-up steel beam at the north end.

The floor system was supported on Teflon slide bearings on steel gravity frames. The LFRS base was attached to the laboratory strong floor through a steel connection. Section AA shows BRB#1 or BRB#2. The RB is shown in sections AA and BB. One side of each RB is attached to the floor system, and the other side of the RB is attached to the LFRS by using threaded rods. The motion of the floor system in the NS direction deformed the BRB axially and deformed the RB in shear. The BRB was in tension when the actuators were extended toward the north and in compression when the actuators were retracted toward the south. A description of the test setup details is presented in [3].

## 3. DEFORMABLE CONNECTION DESIGN

### *3.1. Buckling-restrained brace*

Figure 2(a) shows the BRB components, and Figure 2(b) shows one of the two BRBs installed in the experimental setup. BRB#1 and BRB#2 had the same nominal dimensions and material properties. Table I lists key dimensions of the BRBs. Symbols $t$, $b$, and $L$ with the appropriate subscript denote the thickness, width, and length, respectively, of the yielding zone, transition zone, knife plates, and clevis plates. The yielding zone steel material was American Society for Testing Materials (ASTM) A36 steel [4]. One yielding zone plate was used. $L_{yz}$ was determined from a 2.2% axial strain design limit, assuming that the BRB design deformation demand equals 50 mm. The steel modulus of elasticity $E_s$, the nominal material yielding stress $F_{yn}$, the actual material yielding stress $F_{ya}$ (based on steel coupon test results provided by the BRB manufacturer), the expected nominal yielding force $P_{by,n}$, the expected actual yielding force $P_{by,a}$, and the material overstrength factor $R_y$ (equal to the ratio of $F_{ya}$ to $F_{yn}$) are given in Table II.

The force in the BRB during the experiments, denoted as $P_b$, was directly measured by using a pin load cell, which was installed at the south clevis of the BRB, see Figure 2(c). Positive $P_b$ indicates tension in the BRB. Three linear variable displacement transducers (LVDTs) were used to measure

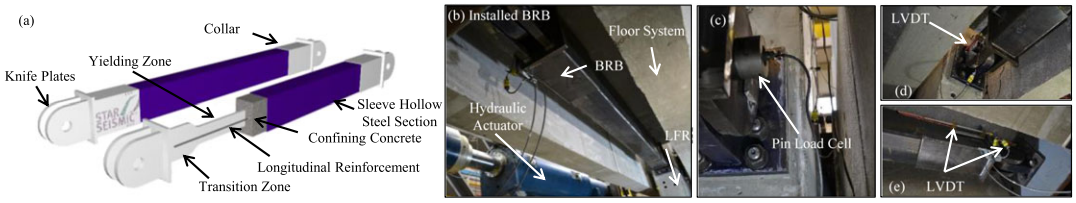



Figure 2. (a) Components of buckling-restrained brace (BRB); (b) BRB in test setup; (c), (d), and (e) BRB instrumentation.

Table I. Buckling-restrained brace component dimensions.

| Yielding zone | | | Transition zone | | | Knife plates | | | Clevis plates | | |
|---|---|---|---|---|---|---|---|---|---|---|---|
| $t_{yz}$ [mm] | $b_{yz}$ [mm] | $L_{yz}$ [m] | $t_{tz}$ [mm] | $b_{tz}$ [mm] | $L_{tz}$ [mm] | $t_{kp}$ [mm] | $b_{kp}$ [mm] | $L_{kp}$ [mm] | $t_c$ [mm] | $b_c$ [mm] | $L_c$ [mm] |
| 25.4 | 139.2 | 2.3 | 25.4 | 250.4 | 398.8 | 38.1 | 330.2 | 368.3 | 63.5 | 330.2 | 374.7 |

Table II. Material properties and strength of buckling-restrained brace yielding zone.

| Material | $E_s$ [GPa] | $F_{yn}$ [MPa] | $F_{ya}$ [MPa] | $P_{by,n}$ [kN] | $P_{by,a}$ [kN] | $R_y = F_{ya}/F_{yn}$ [—] |
|---|---|---|---|---|---|---|
| ASTM A36 | 200 | 248 | 282 | 876 | 996 | 1.14 |

Copyright © 2016 John Wiley & Sons, Ltd.

DOI: 10.1002/eqe

the axial deformation of the BRB. Figure 2(d) and (e) shows the LVDT at each BRB end that was used to measure the total deformation of the knife plate and clevis connection and the motion due to the fabrication tolerance for the clevis plate pin hole and pin diameter. This tolerance was −0/+0.8 mm within the clevis at each end. The third LVDT measured the collar-to-collar deformation of the BRB, see Figure 2(e). The summation of the three LVDT measurements is the BRB deformation, denoted as $D_b$. The yielding zone deformation, denoted as $D_b^{yz}$, is the measured collar-to-collar deformation. Positive $D_b$ and $D_b^{yz}$ indicate displacement of the floor system relative to the LFRS toward the north.

### *3.2. Steel-reinforced laminated low-damping rubber bearings*

Each RB had four laminated rubber layers, approximately 12.5 mm each, with steel reinforcing shims. The thickness of the steel reinforcing shims between the rubber layers was 2 mm. The external rubber layers were bonded to two steel endplates. Neoprene 50±5 Duro Gr. 3 rubber was used. Upper and lower bounds for the rubber shear modulus $G$ are provided by AASHTO [5]. Table III lists the dimensions and the expected properties of each RB based on the upper bound $G$. $W$ and $L$ are the plan dimensions of the rubber; $A$ is the area of the rubber $WL$; $h_{rt}$ is the total thickness of the four rubber layers; $n_L$ is the number of rubber layers; $S$ is the shape factor of the rubber layers; $K_{RB}$ is the elastic shear stiffness of the rubber bearing; $E_c$ is the compressive modulus of the rubber bearing, and $K_c$ is the compressive stiffness of the rubber bearing. The expected total shear stiffness of the four RB is $4K_{RB} = 8.8$ kN/mm. In the experiment, the total RB shear force in the four RB was measured indirectly by subtracting the force measured in the BRB load cell from the sum of the forces in the two actuators.

## 4. TEST PROGRAM

### *4.1. Description of deformable connection tests*

Nine tests were conducted on each BRB+RB connection specimen. Figure 3 shows the deformation histories applied to the BRB#1+RB and BRB#2+RB connection specimens. The lower $x$-axis shows the test number; the upper $x$-axis shows the peak relative velocity (i.e. connection deformation rate)

Table III. Dimensions and nominal properties of rubber bearing.

| $W$ [mm] | $L$ [mm] | $h_{rt}$ [mm] | $n_L$ [—] | $h_{ri}=h_{ri}/n_L$ [mm] | $S=A/[2h_{ri}(W+L)]$ [—] | $G$ [MPa] | $K_{RB}=GA/h_{rt}$ [kN/mm] | $E_c=6GS^2$ [MPa] | $K_c=E_cA/h_{rt}$ [kN/mm] |
|---|---|---|---|---|---|---|---|---|---|
| 356 | 356 | 50 | 4 | 12.5 | 7.0 | 0.9 | 2.2 | 264 | 656 |

Note: Area of the rubber $A = WL$.

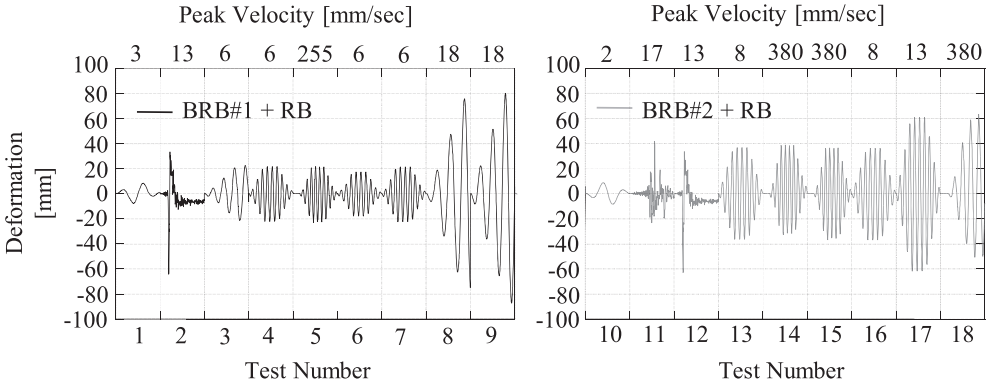



Figure 3. Deformable connection deformation histories and peak velocity for each test.

Copyright © 2016 John Wiley & Sons, Ltd.

DOI: 10.1002/eqe

during the test, and the $y$-axis shows the total BRB deformation $D_b$ that is essentially equal to the RB shear deformation. Table IV summarizes the purpose of each test. More details about the test program are provided in [3].

Test 1 identified the experimental yielding force of BRB#1 in compression. Test 2 used a design basis earthquake (DBE) deformation history, applied quasi-statically at a rate 0.1 times the earthquake deformation rate, to assess the BRB#1+RB response to asymmetric cyclic deformation. The deformation history is based on the deformable connection response at the 12th floor of the 12-story building studied in [1]. Test 3 used a quasi-static sinusoidal deformation history that was not completed due to a hydraulic system error. Note, Figure 3 shows the actual applied deformation history from test 3, which is truncated by the system error compared with the full sinusoidal deformation history shown for test 4. Tests 4, 5, 6, and 7 used sinusoidal deformation histories with similar peak deformations (i.e. approximately 20 mm). Test 5 was dynamic, and tests 4, 6, and 7 were quasi-static. The deformation history used in test 4 was repeated in tests 6 and 7 to assess if there was a residual effect on the BRB#1+RB force–deformation response from a previous high-rate deformation history (i.e. in test 5). Test 8 was a large-amplitude (i.e. approximately 80 mm) quasi-static sinusoidal test that was not completed due to a hydraulic system error. This error did not affect the test results, as shown later. Test 9 was successfully completed and led to fracture in the BRB yielding zone. Figure 3 shows the deformation history in test 9 up to the time of BRB fracture.

Test 10 identified the experimental yielding force of BRB#2 in tension. Test 11 used a DBE deformation history, applied quasi-statically at a rate 0.1 times the earthquake deformation rate. Test 12 of BRB#2+RB used the same DBE deformation history applied to BRB#1+RB in test 2. Tests 13 and 16 used quasi-static sinusoidal deformation histories, and tests 14 and 15 used dynamic sinusoidal deformation histories, with similar peak deformations (i.e. about 40 mm). Test 17 used a large-amplitude quasi-static sinusoidal deformation history. Test 18 used a large-amplitude dynamic sinusoidal deformation history that led to BRB fracture.

### *4.2. Deformable connection experimental response*

Figure 4(a) shows the BRB#1+RB and the BRB#1 force–deformation responses in tests 1 and 2. The maximum and minimum forces in BRB#1+RB were 1550 and −1716 kN and in BRB#1 were 1310 and −1252 kN, respectively. Figure 4(b) shows the BRB#2+RB and the BRB#2 force–deformation responses in tests 10, 11, and 12. The maximum and minimum forces for BRB#2+RB were 1597 and −1925 kN and for BRB#2 were 1370 and −1517 kN, respectively. Stable force–deformation responses were observed for both BRB+RB specimens. The comparison of the BRB+RB and the

Table IV. Test program.

| Test | Specimen | Purpose |
|---|---|---|
| 1 | BRB#1+RB | Assess yielding response in compression under quasi-static sinusoidal deformation |
| 2 | BRB#1+RB | Assess quasi-static design earthquake response |
| 3 | BRB#1+RB | Assess small-amplitude quasi-static sinusoidal response |
| 4 | BRB#1+RB | Assess repeatability of small-amplitude quasi-static sinusoidal response |
| 5 | BRB#1+RB | Assess small-amplitude dynamic sinusoidal response |
| 6 | BRB#1+RB | Assess residual effect of dynamic response in quasi-static sinusoidal response |
| 7 | BRB#1+RB | Assess repeatability of small-amplitude quasi-static sinusoidal response |
| 8 | BRB#1+RB | Assess large-amplitude quasi-static sinusoidal response |
| 9 | BRB#1+RB | Assess large-amplitude quasi-static sinusoidal response |
| 10 | BRB#2+RB | Assess yielding response in tension under quasi-static sinusoidal deformation |
| 11 | BRB#2+RB | Assess quasi-static design earthquake response |
| 12 | BRB#2+RB | Comparison of quasi-static design earthquake response with response in test 1 |
| 13 | BRB#2+RB | Assess medium-amplitude quasi-static sinusoidal response |
| 14 | BRB#2+RB | Assess medium-amplitude dynamic sinusoidal response |
| 15 | BRB#2+RB | Assess repeatability of medium-amplitude dynamic sinusoidal response |
| 16 | BRB#2+RB | Assess residual effect of dynamic response in quasi-static sinusoidal response |
| 17 | BRB#2+RB | Assess large-amplitude quasi-static sinusoidal response |
| 18 | BRB#2+RB | Assess large-amplitude dynamic sinusoidal response |

Copyright © 2016 John Wiley & Sons, Ltd.

DOI: 10.1002/eqe

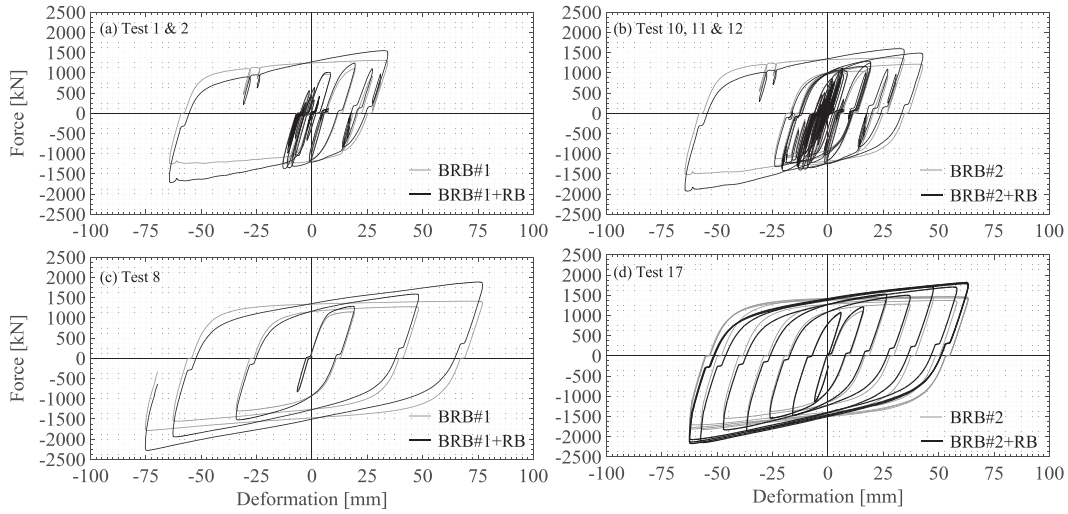



Figure 4. Deformable connection and buckling-restrained brace force–deformation response in quasi-static tests.

BRB peak forces shows the contribution of the RB to the post-elastic stiffness. Test 2 and 12 used the same deformation history, but the forces for BRB#2+RB during test 12 were greater than for BRB#1+RB during test 2 as a result of greater isotropic hardening of BRB#2 from greater deformation demand during the previous tests of BRB#2+RB.

Figure 4(c) shows the BRB #1+RB and the BRB#1 force–deformation response in test 8. The maximum and minimum forces for BRB#1+RB were 1886 and −2277 kN and for BRB#1 were 1410 and −1784 kN, respectively. Figure 4(d) shows the BRB#2+RB and the BRB#2 force–deformation responses in test 17. The maximum and minimum forces for BRB#2+RB were 1808 and −2170 kN and for BRB#2 were 1456 and −1810 kN, respectively. Stable BRB+RB force–deformation response and a significant contribution of the RB to the post-elastic stiffness were also observed in these tests. The BRB#1+RB and BRB#2+RB peak forces are similar in test 8 and test 17, respectively, because significant isotropic hardening of both BRB#1 and BRB#2 has occurred during the previous tests. The pinching deformation observed close to zero force is due to gaps between the BRB pins and BRB clevis plate pin holes due to the fabrication tolerance mentioned earlier. This pinching deformation is 1.6 mm, similar to a standard bolt hole tolerance in construction practice. Numerical simulations in Section 6 show that this pinching deformation does not have an adverse effect on the building seismic response.

Figure 5 shows the progression of hysteretic energy dissipation in BRB#1+RB, BRB#1, BRB#2+RB, and BRB#2 through the experimental program. The figures show that the RB has negligible contribution to the energy dissipation.

Figure 6(a) and (b) shows that the BRB+RB forces under dynamic loading (i.e. test 5 and test 15) are greater than the forces under quasi-static loading (i.e. test 7 and test 16). Near the time of zero deformation, the increase in the BRB+RB force from dynamic loading is 10 to 15%. Figure 6(c) and (d) shows that repetition of quasi-static loading after dynamic loading (i.e. test 4, dynamic loading test 5, and then tests 6 and 7, or test 13, dynamic loading tests 14 and 15, and then test 16) leads to the same force–deformation response with no memory effect from the previous dynamic loading. Because the BRB+RB force–deformation response depends mainly on the BRB response, Section 4.3 provides a detailed discussion of the BRB response.

### *4.3. Buckling-restrained brace experimental response*

In this section, the following six items are discussed: (1) the BRB yielding response; (2) the BRB force–deformation rate dependence; (3) the correlation of BRB isotropic hardening with the maximum plastic deformation range; (4) a backbone BRB force–deformation response fit to the

Copyright © 2016 John Wiley & Sons, Ltd.

DOI: 10.1002/eqe

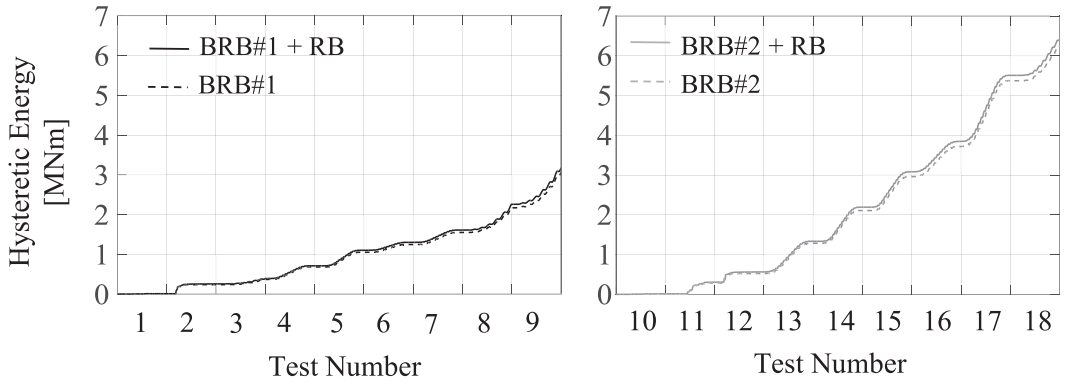



Figure 5. Deformable connection and buckling-restrained brace hysteretic energy dissipation.

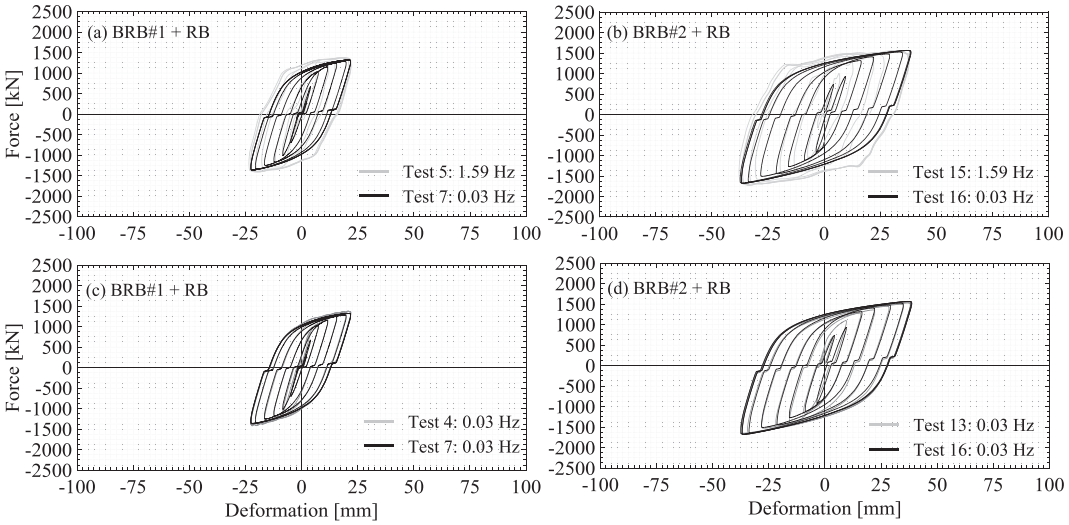



Figure 6. Comparison of quasi-static and dynamic deformable connection response.

experimental data; (5) the BRB overstrength adjustment factors $\omega$ and $\beta$ [6][7]; and (6) fracture and the maximum BRB force.

*4.3.1. Yielding.* Figure 7(a) and (b) shows the force–deformation response in tests 1 and 10, respectively. The BRB force $P_b$ is normalized by $P_{by,a} = 996\,\text{kN}$, and the BRB deformation $D_b$ is normalized by $D_{by,a}$, which is the BRB yielding deformation (rounded to the nearest millimeter) $D_{by,a} = P_{by,a}/K_b = 5\,\text{mm}$, and $K_b$ is the experimental BRB elastic stiffness equal to 185 kN/mm.

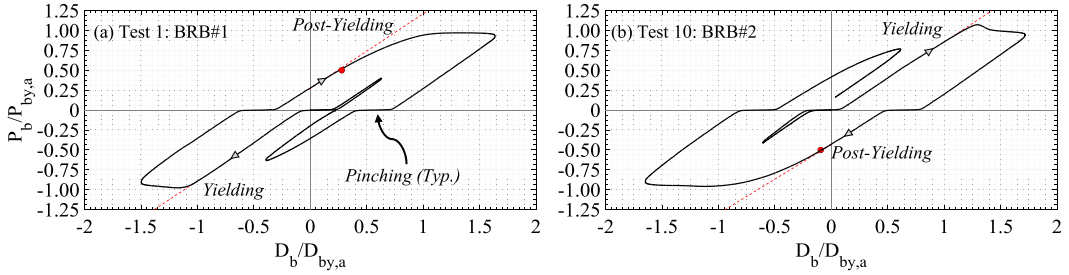



Figure 7. Normalized buckling-restrained brace (BRB) force–deformation plots at yielding (a) BRB#1 first yielding in compression and (b) BRB#2 first yielding in tension.

Copyright © 2016 John Wiley & Sons, Ltd.

DOI: 10.1002/eqe

BRB#1 yields first in test 1 in compression. The experimental yielding force is essentially the same as the calculated actual yielding force $P_{by,a} = 996$ kN. The dashed lines in the figures indicate $K_b$. The initial estimate of the BRB elastic stiffness was 200 kN/mm, based on a series of elastic springs modeling the steel yielding zone, transition zone, knife plates, and clevis plates. Nonlinear post-yielding response in tension initiates at $0.5P_{by,a}$ due to the Bauschinger effect and gradually reaches $P_{by,a}$. The pinching deformation observed at zero force is equal to the total of the gaps between the pins and the clevis plate pin holes due to the fabrication tolerance of −0/+0.8 mm mentioned earlier (i.e. the normalized pinching deformation is $2(0.8\,\text{mm})/D_{by,a}$). A tighter fabrication tolerance between the clevis plates pin holes and pin would lead to less pinching. Figure 7(b) shows that BRB#2 yields first in tension in test 10. Again, the experimental yielding force is essentially the same as $P_{by,a}$, and $K_b$ is 185 kN/mm. The nonlinear post-yielding response in compression initiates at $-0.5P_{by,a}$ due to the Bauschinger effect and gradually reaches $-P_{by,a}$.

*4.3.2. Deformation rate effect.* Figure 8(a) and (b) shows the BRB-normalized force–deformation response in tests 5 and 7 for BRB#1 and in tests 15 and 16 for BRB#2, respectively. The BRB elastic stiffness is not affected by the deformation rate. The post-elastic BRB force near the time of zero deformation in the dynamic tests was 10 to 15% greater than the BRB force near the time of zero deformation in the quasi-static tests. Past research has included similar observations regarding the strain rate effect on ASTM A36 steel [8] [9]. The deformation rate dependence of BRBs has been shown in [10] [11] [12]. Quasi-static tests 4 and 7 for BRB#1 and quasi-static tests 13 and 16 for BRB#2 conducted before and after dynamic tests 5 and 15 led to essentially identical force–deformation response as shown in Figure 8(c) and (d). Considering also the results presented in Figure 6, the greater BRB+RB force in the dynamic tests compared with the quasi-static tests is attributed to the greater BRB force. This greater BRB force should be considered to properly design the components used to attach the BRB of a BRB+RB connection to the LFRS and floor system.

*4.3.3. Buckling-restrained brace isotropic hardening.* The isotropic hardening of the BRB specimens observed in the tests is quantified as the increase in the peak-measured BRB force at zero plastic deformation. In this section, it will be shown that the peak BRB force at zero plastic deformation increases from the initial value of $P_{by,a}$ as the BRB maximum plastic deformation range increases. In past research, isotropic hardening of BRBs has been modeled with hardening 'rules' that govern the evolution of the peak BRB force at zero plastic deformation. A review of these isotropic hardening rules follows.

Researchers have used the cumulative plastic deformation as the main parameter of isotropic hardening rules in BRB force–deformation models. More specifically, Fahnestock et al. [13] [14]

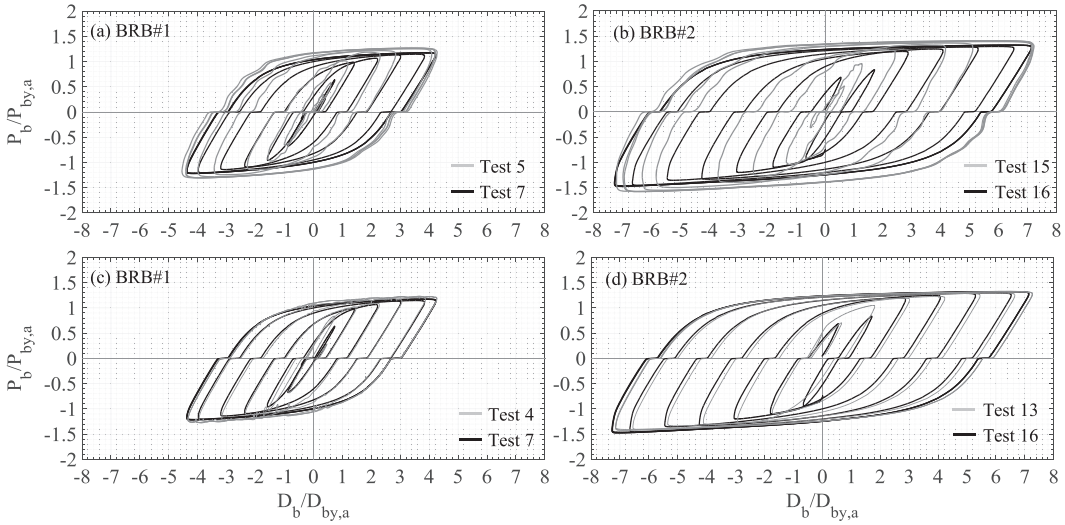



Figure 8. Buckling-restrained brace force–deformation response under quasi-static and dynamic loading history.

Copyright © 2016 John Wiley & Sons, Ltd.

DOI: 10.1002/eqe

proposed a BRB force–deformation model that includes an isotropic hardening rule controlled by the maximum total BRB deformation and the cumulative plastic deformation. The dominant factor in this isotropic hardening rule [13] [14] is the cumulative plastic deformation [13]. Zona and Dall'Asta [15] proposed a BRB force–deformation model in which the cumulative plastic deformation controls the isotropic hardening. The sensitivity of BRB frame response to the parameters of the BRB model developed by Zona and Dall'Asta [15] was studied by Gu et al. [16]. Rossi [17] also used the model proposed by Zona and Dall'Asta [15] to demonstrate the importance of isotropic hardening. Zsarnóczay et al. [18] proposed a BRB force–deformation model in which the cumulative plastic strain controls the isotropic hardening. Karavasilis et al. [19] presented a modified Bouc–Wen model for steel energy dissipation devices that includes an isotropic hardening rule controlled by the cumulative plastic deformation.

More generally, literature on isotropic hardening of steel indicates that hardening is controlled by the plastic strain range. Chaboche et al. [20] presents a model for the cyclic hardening of 316 stainless steel, where the isotropic hardening is controlled by the plastic strain range. Dafalias [21] presented a plasticity model for the response of steel under cyclic loading, in which the isotropic hardening is controlled by the maximum plastic strain range that the material has experienced. Lee et al. [9] tested annealed ASTM A36 steel specimens and showed the dependence of the stress response on the plastic strain range [9].

Menegotto and Pinto presented a stress–strain model for reinforcing steel bars [22]. The model was modified by Filippou et al. [23] to include an isotropic hardening rule that shifts the linear yielding asymptotes (LYAs, see Figure 9) outward, to model the isotropic hardening, based on the maximum absolute strain. This model was implemented in OPENSEES (*Steel02*) [24] with a modification that the isotropic hardening is controlled by the difference between the maximum and minimum strain instead of the maximum absolute strain [24]. Lanning et al. [12] proposed a BRB force–deformation model based on a modified Menegotto–Pinto model [24], where the isotropic hardening is controlled by the cumulative ductility and the difference between the maximum tension and compression ductility levels [12].

This paper uses the BRB force–deformation data from the experimental program to show that the isotropic hardening, quantified as the increase in the peak BRB force at zero plastic deformation, is controlled by the BRB maximum plastic deformation range, $\Delta D^p_{b,max}$. Figure 9 shows schematically that $\Delta D^p_{b,max}$ is the maximum plastic deformation minus the minimum plastic deformation. $\Delta P^0_b$ is the BRB maximum force at zero plastic deformation minus the BRB minimum force at zero plastic deformation. The LYA pass through the maximum (and minimum) possible BRB force at zero plastic deformation after a given value of $\Delta D^p_{b,max}$ has been reached. The slope of the LYA represents the kinematic hardening.

The schematic response in Figure 9 is used to explain the BRB experimental response that is shown in Figures 10 and 11(c). In Figure 9, the initial value of ${}^{(0)}\Delta P^0_b = 2P_{by,a}$, and the initial value of ${}^{(0)}\Delta D^p_{b,max} = 0$. Loading to point A leads to initial yielding. Further loading to point B and load reversal to point C lead to

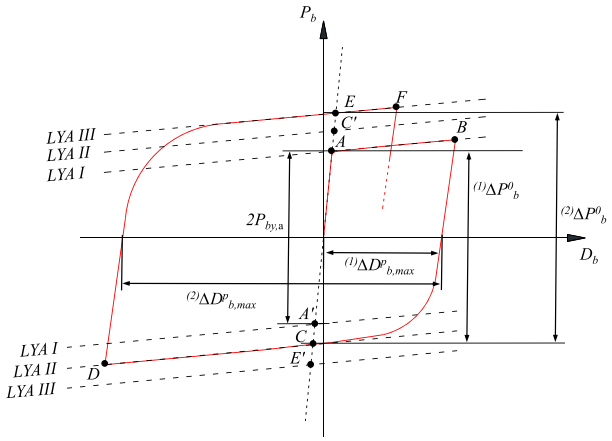



Figure 9. Buckling-restrained brace force–deformation schematic response.

Copyright © 2016 John Wiley & Sons, Ltd.

DOI: 10.1002/eqe

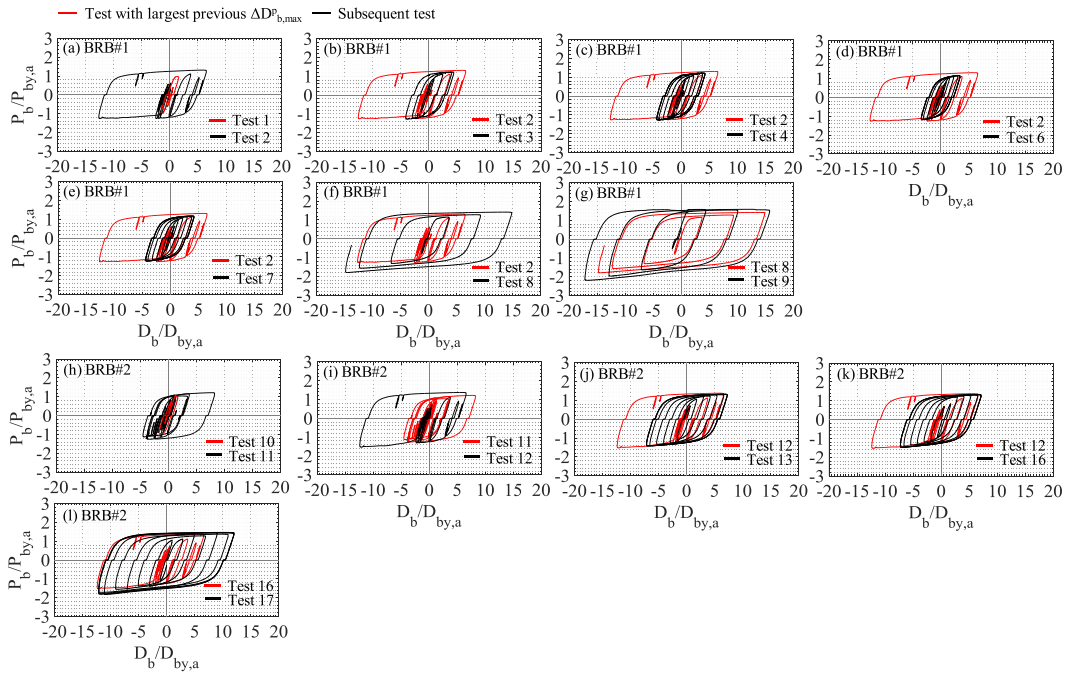



Figure 10. Buckling-restrained brace force–deformation plots showing evolution of peak buckling-restrained brace force at zero plastic deformation in quasi-static tests.

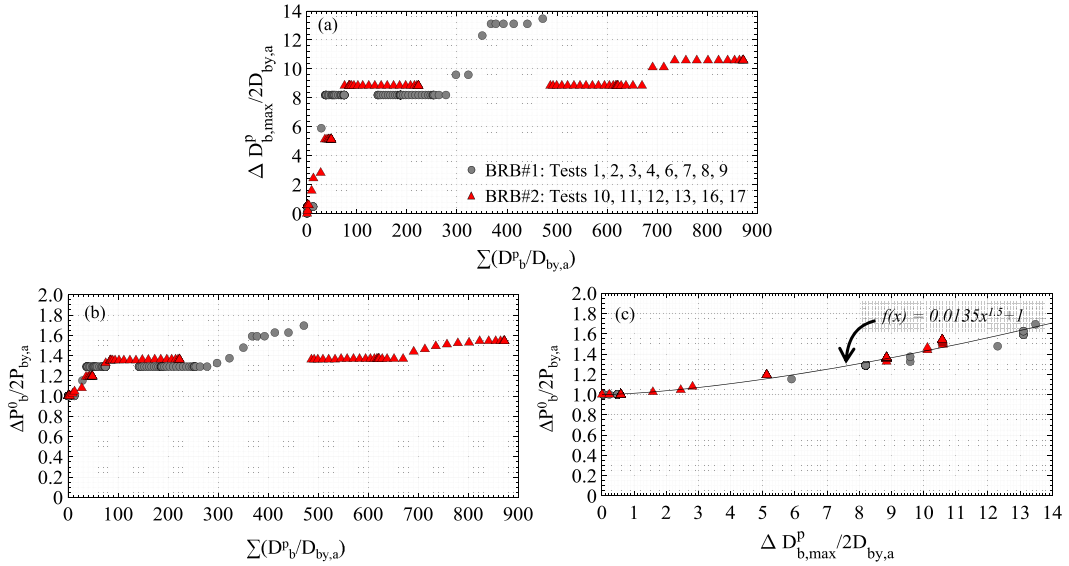



Figure 11. (a) Normalized maximum plastic deformation range versus normalized cumulative plastic deformation, (b) normalized force range at zero plastic deformation versus normalized cumulative plastic deformation, and (c) normalized maximum force range at zero plastic deformation versus normalized maximum plastic deformation for BRB#1 and BRB#2 quasi-static tests.

an updated ${}^{(1)}\Delta D^{p}_{b,max} > {}^{(0)}\Delta D^{p}_{b,max}$ and ${}^{(1)}\Delta P^{0}_{b} > {}^{(0)}\Delta P^{0}_{b}$. Further loading to point D and load reversal to point E lead to ${}^{(2)}\Delta D^{p}_{b,max} > {}^{(1)}\Delta D^{p}_{b,max}$, and ${}^{(2)}\Delta P^{0}_{b} > {}^{(1)}\Delta P^{0}_{b}$. A load reversal at point F would not increase $\Delta D^{p}_{b,max}$. As a result, ${}^{(3)}\Delta D^{p}_{b,max} = {}^{(2)}\Delta D^{p}_{b,max}$, ${}^{(3)}\Delta P^{0}_{b} = {}^{(2)}\Delta P^{0}_{b}$, and the force–deformation curve would approach LYA III if loading continued after the load reversal at point F.

Figure 10 shows the normalized force–deformation responses for BRB#1 and BRB#2 from the quasi-static tests. The red line represents the first test that initial yielding occurred or a previous test

Copyright © 2016 John Wiley & Sons, Ltd.

DOI: 10.1002/eqe

in which the largest previous $\Delta D^p_{b,max}$ was observed. The subsequent test is shown with a black line. Each time the subsequent test increases $\Delta D^p_{b,max}$, the subsequent test becomes the test in which the largest previous $\Delta D^p_{b,max}$ was observed, which is shown with a red line in the next plot. When the subsequent test does not increase $\Delta D^p_{b,max}$, an increase in the peak BRB force at zero plastic deformation is not observed. In Figure 10(a), (f), and (g) for BRB#1 and Figure 10(h), (i), and (l) for BRB#2, the subsequent test increases $\Delta D^p_{b,max}$, and an increased peak BRB force at zero plastic deformation is observed.

Figure 11(a) shows a plot of $\Delta D^p_{b,max}$ normalized by $2D_{by,a}$ versus the cumulative normalized plastic deformation $\sum(D^p_b/D_{by,a})$ for all the quasi-static tests. The circles and the triangles represent the experimental results for BRB#1 and BRB#2, respectively. Each BRB was subjected to some tests that increased $\sum(D^p_b/D_{by,a})$ without increasing $\Delta D^p_{b,max}/2D_{by,a}$. Figure 11(b) shows a plot of $\Delta P^0_b$ normalized by $2P_{by,a}$ versus $\sum(D^p_b/D_{by,a})$. The figure shows that $\Delta P^0_b/2P_{by,a}$ often shows no increase with increasing $\sum(D^p_b/D_{by,a})$, and there is no apparent relationship between $\Delta P^0_b/2P_{by,a}$ and $\sum(D^p_b/D_{by,a})$. Figure 11(c) shows $\Delta P^0_b/2P_{by,a}$ versus $\Delta D^p_{b,max}/2D_{by,a}$. The experimental results for each BRB specimen indicate that $\Delta P^0_b/2P_{by,a}$ increases with increasing $\Delta D^p_{b,max}/2D_{by,a}$. A curve fit to the experimental results is shown in Figure 11(c).

*4.3.4. Backbone curve and overstrength factors.* To properly design the attachments of the BRB to the LFRS and the floor system, the expected peak BRB forces are needed. A backbone curve fit to the BRB force-yielding zone deformation response is used to calculate the standard BRB overstrength adjustment factors $\beta$ and $\omega$ [6] [7]. The compression strength adjustment factor $\beta$ is defined as the ratio of the maximum compression BRB force to the maximum tension BRB force [6]. The tension strength adjustment factor $\omega$ is defined as the ratio of the maximum tension BRB force to $P_{by,a}$ [6]. The overstrength adjustment factors account for isotropic and kinematic hardening in the yielding zone, for friction due to the contact of the yielding zone with the confining concrete in the BRB when the BRB is in compression, and for Poisson's effect [25].

The plots in Figure 12(a) through (d) show $P_b$ normalized by $P_{by,a}$ versus the deformation of the BRB yielding zone $D^{yz}_b$ normalized by $D_{by,a}$. Figure 12(a) shows data from quasi-static tests 1 and 2 of BRB#1. The red circles indicate the local peak $P_b/P_{by,a}$ near the large negative value of $D^{yz}_b/D_{by,a}$ and the local peak $P_b/P_{by,a}$ near the large positive value of $D^{yz}_b/D_{by,a}$. Figure 12(b) shows data from test 7 of BRB#1, which is a typical quasi-static sinusoidal test. The local peak $P_b/P_{by,a}$ values in each half cycle are shown with white circles. Figure 12(c) shows data from quasi-static tests 10 and 11 of BRB#2. The red triangles indicate the local peak $P_b/P_{by,a}$ near the large negative value of $D^{yz}_b/D_{by,a}$ and the local peak $P_b/P_{by,a}$ near the large positive value of $D^{yz}_b/D_{by,a}$. Figure 12(d) shows data

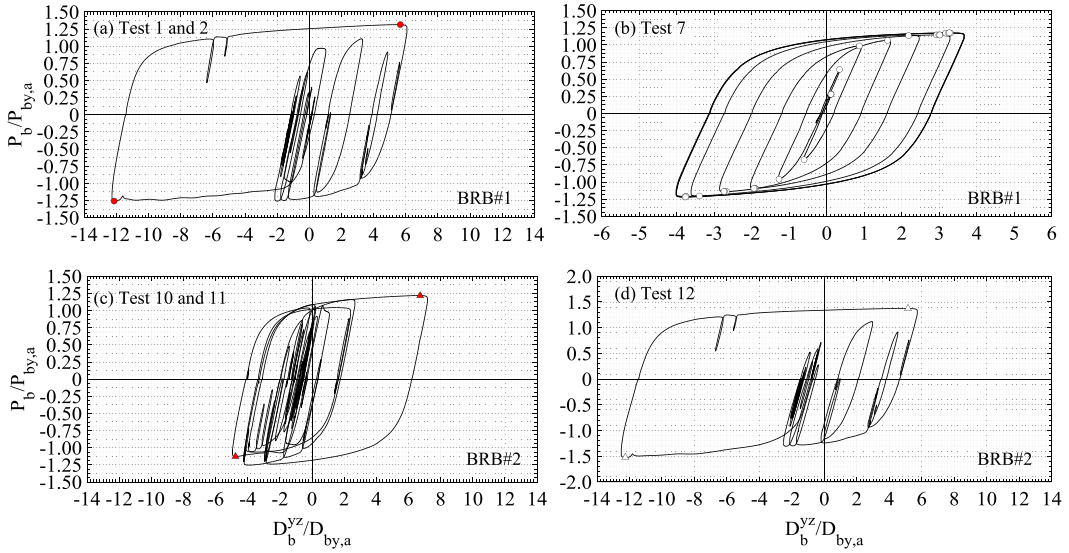



Figure 12. Normalized buckling-restrained brace force versus yielding zone deformation and peak response data.

Copyright © 2016 John Wiley & Sons, Ltd.

DOI: 10.1002/eqe

from quasi-static test 12 of BRB#2. BRB#2 experienced significant isotropic hardening in test 11. Similar to Figure 12(a), the white triangles in Figure 12(d) indicate the local peak $P_b/P_{by,a}$ near the large negative value of $D_b^{yz}/D_{by,a}$ and the local peak $P_b/P_{by,a}$ near the large positive value of $D_b^{yz}/D_{by,a}$.

Figure 13(a) shows the selected local peak $P_b/P_{by,a}$ versus $D_b^{yz}/D_{by,a}$ data from Figure 12(a), (c), and (d), and the local peak $P_b/P_{by,a}$ versus $D_b^{yz}/D_{by,a}$ data from all quasi-static sinusoidal tests similar to that shown in Figure 12(b). The upper $x$-axis in Figure 13(a) shows the yielding zone strain, $\varepsilon_{yz} = D_b^{yz}/L_{yz}$. The white circles and triangles are peak $P_b/P_{by,a}$ values *after significant isotropic hardening has occurred*, as observed by comparing the peak $P_b/P_{by,a}$ when $D_b^{yz}/D_{by,a}$ is approximately equal to $-12$; $P_b/P_{by,a}$ at the large negative value of $D_b^{yz}/D_{by,a}$ from test 2 (i.e. red circle) is smaller than the peak $P_b/P_{by,a}$ values from other tests, because *significant isotropic hardening has not occurred*. When $D_b^{yz}/D_{by,a}$ is approximately equal to 6, the tensile peak $P_b/P_{by,a}$ from test 2 (i.e. red circle) is similar to the peak $P_b/P_{by,a}$ values from other tests, because *significant isotropic hardening has occurred*. The white circles and triangles (i.e. after significant isotropic hardening) are used to fit a backbone curve to the peak BRB force–deformation data.

When $P_b$ is in tension, the values of $P_b/P_{by,a}$ that are larger than 1.0 in Figure 13(a) give the tension strength adjustment factor $\omega$ [6] [7]. The black line in Figure 13(b) shows $\omega$ versus $D_b^{yz}/D_{by,a}$ based on the backbone curve. When $P_b$ is in compression, the absolute values of $P_b/P_{by,a}$ that are larger than 1.0 give the compression strength adjustment factor $\beta$ multiplied by the tension strength adjustment factor $\omega$ [6] [7]. Figure 13(c) shows $\beta\omega$ versus $D_b^{yz}/D_{by,a}$. Figure 13(d) shows $\beta$ versus $D_b^{yz}/D_{by,a}$ where $\beta$ has been calculated as $\beta\omega/\omega$ by using the values from the backbone curve fit. Note that $\beta$ is less than the limit of 1.3 given in [6]. For comparison, Figure 13(b) and (d) also shows with dashed grey lines the regression formulas proposed by Saxey et al. [25], which give $\omega = 20.63\varepsilon_{yz} + 1.04$ and $\beta = 4.96\varepsilon_{yz} + 1.02$, where $\varepsilon_{yz}$ is equal to $(D_b^{yz}/D_{by,a})(D_{by,a}/L_{yz})$. Note that the regression results from [25] are based on data from 39 full-scale tests of various types of BRBs, while the results here are based on data for two BRBs with the same BRB design after significant isotropic hardening has occurred (with the deformation rate effect excluded).

*4.3.5. Fracture and absolute maximum buckling-restrained brace force.* Figure 14(a) and (b) shows the normalized force–deformation response, for BRB#1 and BRB#2, respectively, for the tests in which fracture occurred. The BRBs fractured while they were in tension, close to zero $D_b/D_{by,a}$. BRB#1 fractured during quasi-static test 9. Before fracture, it was subjected to a peak $D_b/D_{by,a}$ of

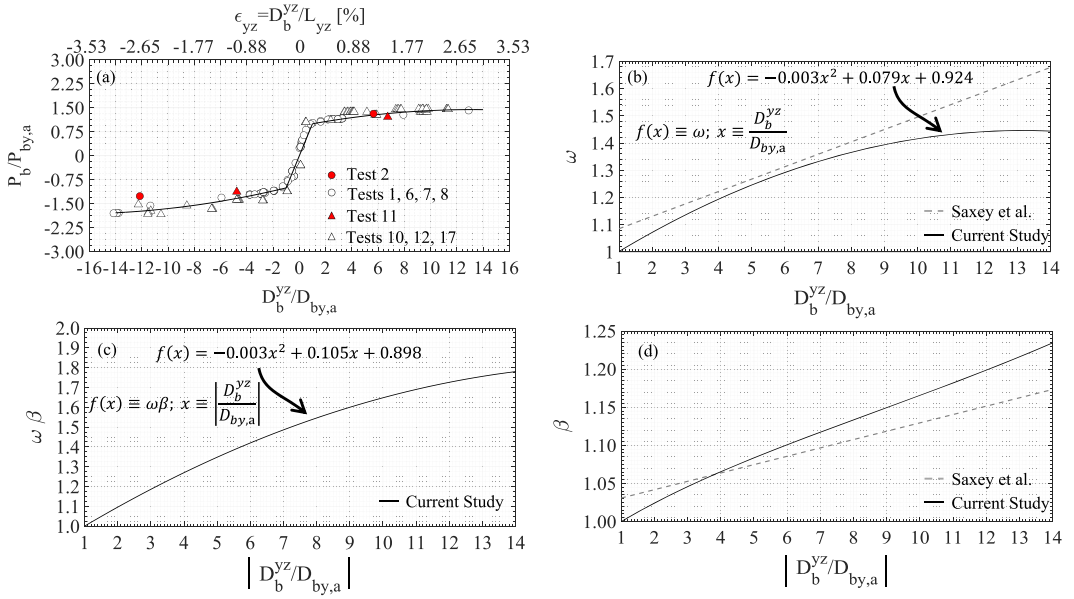



Figure 13. Peak buckling-restrained brace response data, backbone curve, and overstrength adjustment factors.

Copyright © 2016 John Wiley & Sons, Ltd.

DOI: 10.1002/eqe

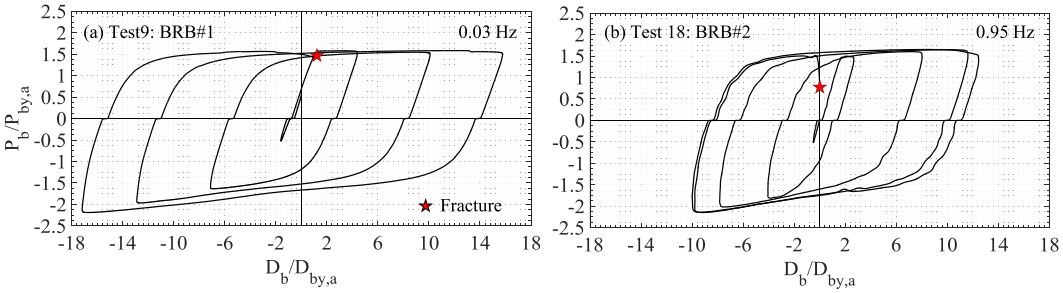



Figure 14. Fracture of buckling-restrained braces.

approximately 17 (a peak $\varepsilon_{yz}$ of about 3.8%), $\sum(D_b/D_{by,a})$ was approximately 470, the total hysteretic energy dissipated was approximately 3 mNm, and the peak $\Delta D^p_{b,max}/2D_{by,a}$ was approximately 14. BRB#2 fractured during dynamic test 18. Before fracture, it was subjected to a peak $D_b/D_{by,a}$ of approximately 12 (a peak $\varepsilon_{yz}$ of about 2.8%), $\sum(D_b/D_{by,a})$ was approximately 870, the total hysteretic energy dissipated was approximately 6 mNm, and the peak $\Delta D^p_{b,max}/2D_{by,a}$ was approximately 11.

The ultimate tensile stress of ASTM A36 steel $F_u$ is expected to vary over a range from 400 to 550 MPa [4]; therefore, $F_u/F_{ya} = (A_{yz}F_u)/(A_{yz}F_{ya}) = P_{bu}/P_{by,a}$ is expected to be between 1.42 and 1.95, where $P_{bu}$ is the expected BRB force at the ultimate tensile stress. From the tests, the largest tensile $P_b/P_{by,a}$ was 1.58 and 1.65 for BRB#1 and BRB#2, respectively. The largest compressive $P_b/P_{by,a}$ was −2.19 and −2.14 for BRB#1 and BRB#2, respectively, which are greater in absolute value than the largest expected value of $P_{bu}/P_{by,a}$ (i.e. 1.95). Friction from contact of the yielding zone with the confining concrete in the BRB when the BRB is in compression and the Poisson effect [25] [26] may contribute to these large $P_b/P_{by,a}$ values. Note that data from dynamic tests and tests that led to fracture are not included in plots shown in Figure 13(a) through (d), and the associated overstrength factor results do not account for the deformation rate effect nor the friction and Poisson effect at large deformations near fracture of the BRB.

## 5. DEFORMABLE CONNECTION FORCE–DEFORMATION NUMERICAL MODEL

The force–deformation response of the BRB+RB deformable connection was modeled in OPENSEES [27], and the response of the model was compared with the experimental response. Figure 15(a) shows a truss element that was used to model the BRB+RB connection. The length of the truss element is equal to the length of the BRB, $L_{truss} = L_{yz} + 2L_{tz} + 2L_{kp} + 2L_c = 4584$ mm. A unit area was specified for the truss, $A_{truss} = 1\ \text{mm}^2$. OPENSEES enables springs to be modeled as uniaxial stress–strain materials, which can be assigned to the truss element, where the spring force normalized by $A_{truss}$ is the uniaxial stress of the material, and the spring deformation normalized by $L_{truss}$ is the uniaxial strain of the material. Two internal springs in series (Figure 15(b)) were used to model the BRB force–deformation response within the truss element. The BRB yielding zone spring was modeled by using the *Steel02* [24] uniaxial material (Figure 15(c)), with parameters $F_y$, $E0$, $b$, $R0$, $cR1$, $cR2$, $a1$, $a2$, $a3$, and $a4$ equal to $P_{by,a}/A_{truss} = (F_{ya}A_{yz})/A_{truss}$, $K_{yz}(L_{truss}/A_{truss}) = E_s(A_{yz}/L_{yz})(L_{truss}/A_{truss})$, 0.01, 30.00, 0.95, 0.15, 0.03, 1.00, 0.04, and 1.00, respectively. The parameter $b$ is the ratio between the post-elastic stiffness and the elastic stiffness of the BRB yielding zone spring. Constant kinematic hardening is used in the *Steel02* uniaxial material. The parameters $R0$, $cR1$, and $cR2$ control the transition from elastic to post-elastic stress–strain response. The parameters $\alpha 1$ and $\alpha 2$ control the isotropic hardening in compression, and $\alpha 3$ and $\alpha 4$ control the isotropic hardening in tension. It is worth noting that isotropic hardening in the *Steel02* uniaxial material is based on the maximum total strain (i.e. elastic strain + plastic strain) range [24]. Thus, the BRB yielding zone spring uses the BRB maximum total deformation range instead of the BRB maximum plastic deformation range. However, comparisons of the force–deformation response from the BRB+RB

Copyright © 2016 John Wiley & Sons, Ltd.

DOI: 10.1002/eqe

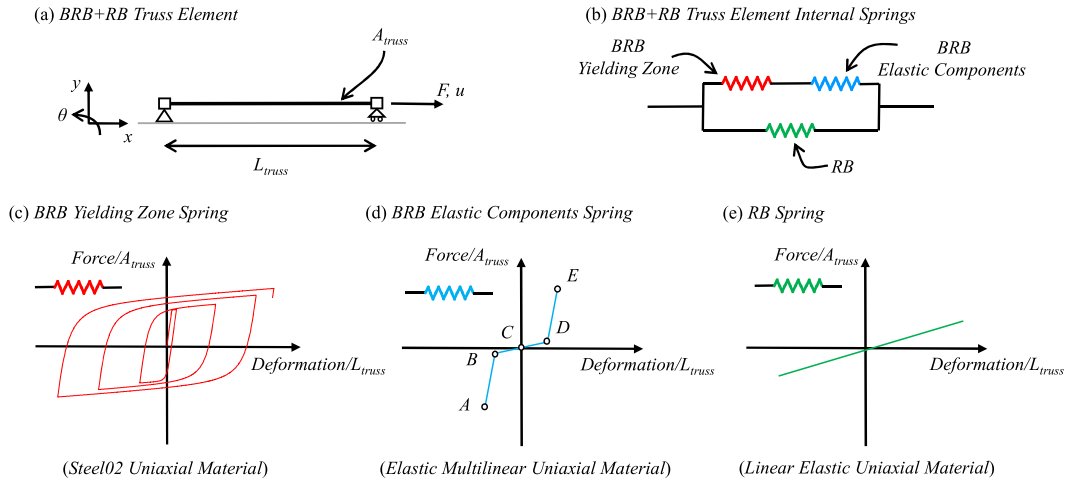



Figure 15. (a) Deformable truss element, (b) series and parallel internal springs, (c) buckling-restrained brace yielding zone spring response, (d) buckling-restrained brace elastic component spring response, and (e) rubber bearings spring response.

model with the test results show that this simplification in the isotropic hardening model does not lead to significant error in the force–deformation response.

The elastic components of the BRB and the pinching deformation at zero BRB force (related to the fabrication tolerance for the clevis plate pin hole and pin diameter) were modeled as an elastic multilinear [28] uniaxial material, with the stress–strain response shown in Figure 15(d). For this response, the slope of segments AB and DE equals $K_{eqel}/(L_{truss}/A_{truss})$ (where $K_{eqel}$ is given by Eqns (1) and (2)), and the slope of segment BCE equals 1% of the slope of segments AB and DE. Points B and D are at one-half of the normalized pinching deformation, $-0.8/L_{truss}$ and $+0.8/L_{truss}$, respectively. Also within the truss element, the RB was modeled as a linear elastic spring in parallel with the springs in series that model the BRB (Figure 15(b)), and this spring was modeled as a linear elastic uniaxial material (Figure 15(e)) with a modulus of 8 kN/mm ($L_{truss}/A_{truss}$).

$$K_{eqel} = \frac{K_c K_{kp} K_{tz}}{2K_{kp}K_{tz} + 2K_{kp}K_c + 2K_c K_{tz}} \tag{1}$$

$$K_c = \frac{E_s t_c b_c}{L_c}; \cdot K_{kp} = 2\frac{E_s t_{kp} b_{kp}}{L_{kp}}; \cdot K_{tz} = \frac{E_s t_{tz} b_{tz}}{L_{tz}} \tag{2}$$

Figure 16(a) compares the numerical and the experimental BRB+RB force–deformation responses for tests 1 and 2. Figure 16(b) compares the hysteretic energy dissipation histories. Figure 16(c) and (d) compares the numerical model force–deformation and hysteretic energy dissipation for tests 10, 11, and 12. The results show that the numerical model accurately represents the BRB+RB force–deformation response.

Figure 17(a) compares the numerical and experimental BRB+RB force–deformation responses for tests 1, 2, and 8. Test 8 had a much larger deformation range than tests 1 and 2, and the comparisons for test 8 show some limitations of the numerical model. Figure 17(b) compares the numerical and experimental RB force–deformation responses in test 8. Figure 17(c) compares the numerical and experimental BRB force–deformation responses in the large cycles in test 8. The difference between the numerical and experimental BRB+RB force in Figure 17(a), as the deformation approaches +80 mm, is attributed mainly to the difference between the linear elastic RB model response and the experimental RB response during large deformations, shown in Figure 17(b). Figure 17(c) shows the BRB model with constant kinematic hardening, as discussed earlier, which differs from the stiffness softening in tension and stiffness hardening in compression (see also Section 4.3.5) observed in the BRB experimental results. The differences between the numerical and experimental BRB+RB forces near zero deformation, after the deformation reversal from

Copyright © 2016 John Wiley & Sons, Ltd.

DOI: 10.1002/eqe

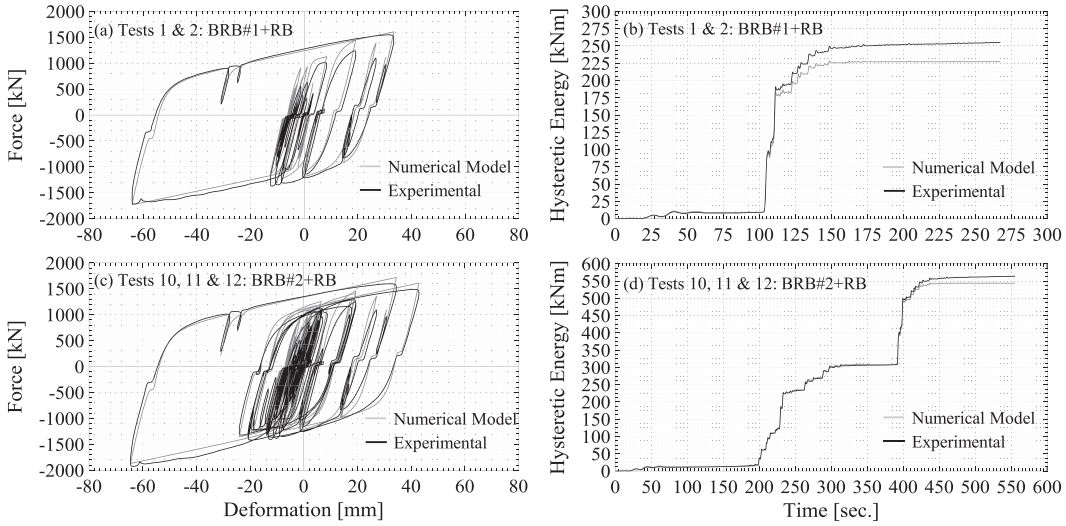



Figure 16. Deformable numerical model with experimental results.

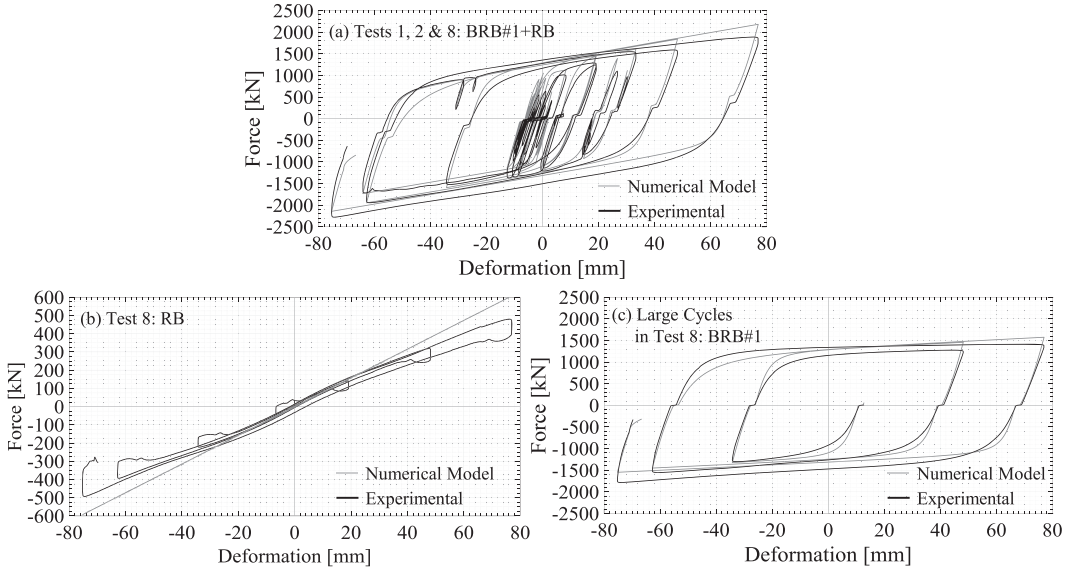



Figure 17. (a) Comparison of deformable numerical model with experimental results from selected quasi-static tests, (b) comparison of rubber bearings numerical model with experimental results, and (c) comparison of buckling-restrained brace numerical model with experimental results for large deformation cycles.

approximately +80 mm, is mainly attributed to inaccuracy in the numerical model isotropic hardening rule at these large deformations. It is noted that the numerical model does not include the deformation rate dependence or fracture of the BRB. Despite these limitations of the model, it is considered to be sufficiently accurate for the application presented in this paper.

## 6. NUMERICAL SIMULATIONS AT SYSTEM LEVEL

Numerical simulations of the seismic response of a 12-story reinforced concrete shear wall building with BRB+RB deformable connections were carried out with the following objectives: (1) to assess the effect of the stiffness provided by the RB on the seismic response of the building and (2) to assess the effect of

Copyright © 2016 John Wiley & Sons, Ltd.

DOI: 10.1002/eqe

BRB isotropic hardening on the seismic response of the building. The building model, described in [1], was used, and it has identical BRB+RB connections between each floor and the shear wall. As noted in [1], a damping coefficient was not assigned to the wall base nonlinear spring or to the elements that represent the deformable connections. In the baseline model, the BRB+RB connections are modeled by using the experimentally validated numerical model described in Section 5. The seismic response of the baseline model is compared with the response of a building model that has BRB+RB connections without isotropic hardening in the BRB and with the response of a building model that has BRB-only connections (i.e. without RB) between the floors and shear wall.

In the following figures and discussion, *BRB+RB* denotes the building model with the experimentally validated model for the BRB+RB connections, *BRB NH+RB* denotes the building model that includes a BRB+RB connection model without isotropic hardening in the BRB, and *BRB* denotes the building model with the BRB-only connection model that does not include the stiffness of the RB. The comparison of the BRB+RB building model results with the BRB NH+RB building model results shows the importance of BRB isotropic hardening to the seismic response. The comparison of the BRB+RB building model results with the *BRB* building model results shows the importance of the RB elastic shear stiffness to the seismic response.

Eighteen ground motions were selected from the FEMA P-695 [29] far field set and used as input to the numerical earthquake simulations as discussed in [1]. The average method [30] was used to scale the recorded ground motions, so the spectral accelerations matched the ASCE7-10 [31] DBE spectrum over a range of periods T∈ [0.6, 2.0] seconds.

Figure 18(a) shows the 12th floor connection force–deformation responses for each building model subjected to a ground motion from the 1978 Superstition Hills earthquake (El Centro ICC000 record). The BRB NH+RB building model has a larger connection deformation demand than the BRB+RB building model. The BRB NH+RB and BRB+RB building models have similar peak connection forces. The *BRB* building model (without the RB) has a significantly larger connection deformation demand than the BRB+RB building model and a smaller peak connection force than the BRB+RB building model. The peak BRB force in the *BRB* building model, however, is larger than the peak BRB force in the BRB+RB building model (where, for the BRB+RB building model, the RB force at the peak deformation of 80 mm is 8 kN/mm × 80 mm = 640 kN). Figure 18(b) shows time histories of connection deformation. The BRB NH+RB and the BRB+RB building models have similar residual connection deformations. The BRB building model has a significantly larger residual connection deformation than the BRB+RB building model.

Figure 19 compares the peak story/floor responses for each ground motion and the mean response values for all 18 ground motions for the BRB NH+RB, BRB+RB, and BRB building models. Figure 19(a) shows that the peak LFRS story shears, and the mean values are similar for all three building models with approximately 5% difference between the BRB and the BRB+RB building models. Figure 19(b) shows the peak connection force transferred from the floor system to the LFRS. The BRB building model has smaller mean peak connection forces than the BRB+RB building model at every floor. A 15% difference in mean peak connection force is observed for the three upper floors. The mean peak connection forces for the BRB NH+RB and BRB+RB building models are similar. Figure 19(c) and (d) shows that the peak LFRS story drifts and peak GLRS story drifts, as well as the corresponding mean peak story drifts, are similar for the three building

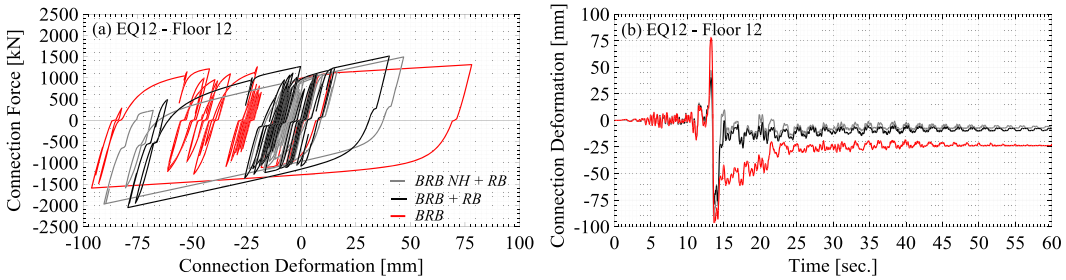



Figure 18. Twelfth floor connection responses for BRB NH+RB, BRB+RB, and BRB building models: (a) force–deformation responses and (b) deformation time histories.

Copyright © 2016 John Wiley & Sons, Ltd.

DOI: 10.1002/eqe

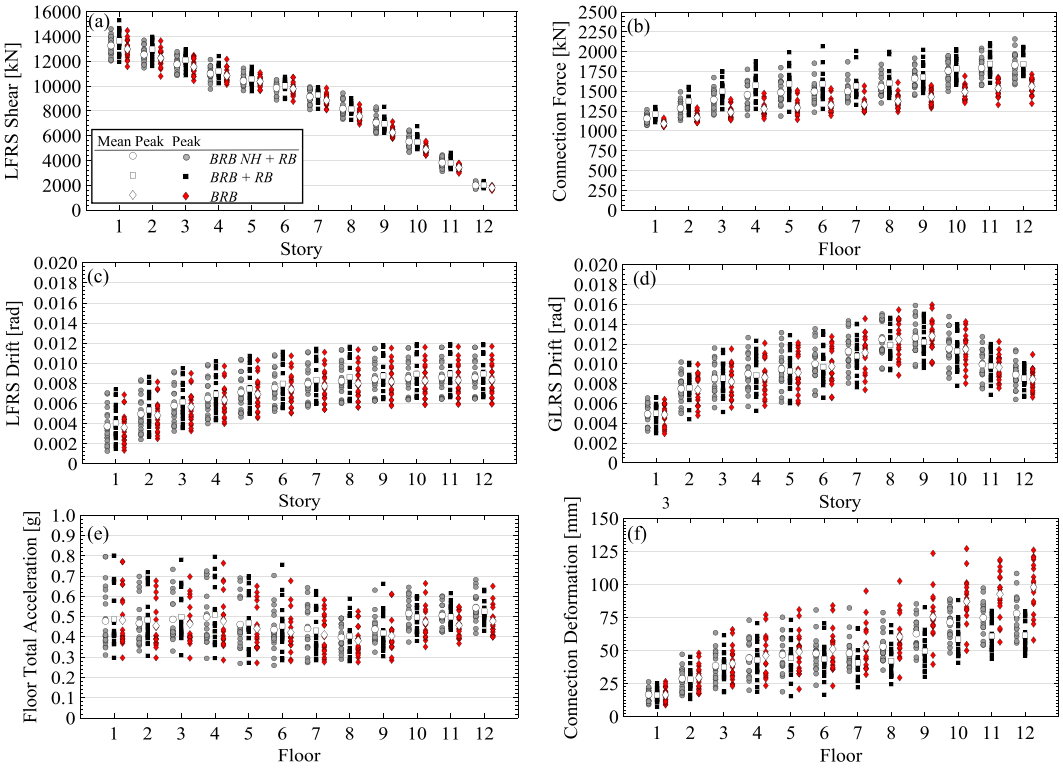



Figure 19. Numerical simulation results.

models. Figure 19(e) shows that the peak floor total accelerations are similar for the three building models. Figure 19(f) shows that the mean peak connection deformations for BRB building model are greater than those of the BRB+RB building model at every floor. The 12th floor connection in the BRB building model has 60% greater mean peak deformation than the 12th floor connection in the BRB+RB building model. The 12th floor connection in the BRB NH+RB building model has a mean peak deformation that is 20% greater than that of the BRB+RB building model.

In summary, for DBE-level ground motions, the LFRS story shears, LFRS story drifts, GLRS story drifts, and floor total accelerations are not significantly affected by either the isotropic hardening of the BRB or the elastic shear stiffness of the RB in the BRB+RB deformable connection force–deformation model. However, the connection deformation demands are significantly smaller in the upper floors of the building model that includes both isotropic hardening of the BRB and the RB stiffness in the BRB +RB deformable connection model. In addition, a mean absolute 12th floor residual connection deformation of 20 mm was observed for the BRB building model, while a mean absolute 12th floor residual connection deformation of only 5 mm was observed for the BRB+RB building model. Thus, including the RB stiffness in the connection model reduces the connection deformation and reduces the residual connection deformation. A BRB+RB connection model with BRB isotropic hardening provides more accurate connection deformation predictions compared with a BRB+RB connection model without BRB isotropic hardening.

## 7. CONCLUSIONS

This paper has presented experimental and numerical studies of a full-scale deformable connection used to connect the floor system of the flexible GLRS to the stiff LFRS of an earthquake-resistant building. The purpose of the deformable connection is to limit the earthquake-induced horizontal inertia forces transferred from the floor system to the LFRS. The deformable connection that was studied consists of a BRB and RB and is denoted as the BRB+RB connection. Details of two

Copyright © 2016 John Wiley & Sons, Ltd.

DOI: 10.1002/eqe

BRB+RB connection test specimens have been presented. Each specimen was subjected to quasi-static earthquake and sinusoidal deformation histories and dynamic sinusoidal deformation histories.

Detailed experimental results for BRB+RB connections have been presented. The experimental response of the BRB, which dominated the BRB+RB connection force–deformation response, was extensively discussed, including the response under various types of deformation histories, and a detailed discussion of the BRB isotropic hardening and the relationship of this hardening to different deformation parameters. Details and limitations of a validated, accurate model for the BRB+RB connection force–deformation response were presented. Numerical simulations by using this model were conducted to assess the effects of different models of the BRB+RB connection force–deformation response on the seismic response of a 12-story reinforced concrete wall building model, and the effects of the BRB isotropic hardening and the RB stiffness were shown.

The experimental and limited numerical studies show that

1. A BRB+RB connection can be fabricated and attached to the floor system and LFRS by using components that are commonly used in building construction.
2. Stable and predictable nonlinear force–deformation response was observed for the BRB+RB connection specimens in tests with quasi-static and dynamic deformation histories.
3. Isotropic hardening of the BRB, quantified as an increase in the BRB force at zero plastic deformation under cyclic loading, depends on the maximum plastic deformation range experienced by the BRB.
4. The BRB+RB connection force response under dynamic deformation histories is 10 to 15% greater than the force response under quasi-static deformation histories, and this greater force should be considered when the components used to attach the BRB to the floor system and the LFRS are designed.
5. The observed quasi-static experimental force–deformation response of the BRB+RB connection can be modeled accurately by using a truss element and a set of uniaxial material models available in OPENSEES. The increased BRB force response under dynamic deformation histories and fracture of the BRB were not included in the models.
6. Including the RB in the BRB+RB connection reduces the connection deformation and the residual connection deformation due to the influence of the RB elastic shear stiffness after the BRB yields.
7. Including the RB in the BRB+RB connection does not significantly affect the floor total accelerations, the LFRS story shears, the LFRS story drifts, or the GLRS story drifts.
8. Including the BRB isotropic hardening in the BRB+RB connection force–deformation model does not significantly affect the LFRS story shears, the LFRS story drifts, or the GLRS story drifts; however, the peak BRB+RB connection deformation is predicted more accurately when the model includes BRB isotropic hardening.

## ACKNOWLEDGEMENTS

This paper is based upon work supported by grants from the National Science Foundation, Award No. CMMI-1135033 in the George E. Brown, Jr. Network for Earthquake Engineering Simulation Research (NEESR) program and Award No. CMMI-0402490 for the George E. Brown, Jr. Network for Earthquake Engineering Simulation (NEES) consortium operations. The authors are grateful for additional financial support provided by the Gerondelis Foundation, Yen Fellowship, and Lehigh University. The contributions of Dr Joe Maffei, Mr. David Mar, and the NEES@Lehigh and ATLSS Center staff are acknowledged. The authors appreciate the contributions of DYMAT™ and Star Seismic® and Scan-Pac Mfg, Inc. Any opinions, findings, and conclusions expressed in this paper are those of the authors and do not necessarily reflect the views of the National Science Foundation or others acknowledged here.

## REFERENCES

1. Tsampras G, Sause R, Zhang D, Fleischman RB, Restrepo JI. Development of deformable connection for earthquake-resistant buildings to reduce floor accelerations and force responses. *Earthquake Engineering and Structural Dynamics* 2016; **45**(9):1473–1494.
2. Facility R-TM-DT, Guide U's. *Engineering Research Center for Advanced Technology for Large Structural Systems (ATLSS)*. Bethlehem: PA, 2014.

Copyright © 2016 John Wiley & Sons, Ltd.

DOI: 10.1002/eqe

3. G. Tsampras and R. Sause, Development and experimental validation of deformable connection for earthquake-resistant building systems with reduced floor accelerations, Network of Earthquake Engineering Simulation (NEES) Technical Report, https://nees.org/resources/13612, 2015.
4. ASTM A36/A36M - 14, Standard specification for carbon structural steel, American Society for Testing and Materials, 2014.
5. AASHTO, LRFD Bridge Design Specification, Washington, DC, 2010.
6. AISC. *ANSI/AISC 341 Seismic Provisions for Structural Steel Buildings*. American Institute of Steel Construction: Chicago, Illinois, 2010.
7. BSSC and FEMA, Recommended provisions for seismic regulations for new buildings and other structures (FEMA 450) Part 2: Commentary, Building Seismic Safety Council - National Institute of Building Sciences, Washington, DC, 2003.
8. Chang K-C, Lee GC. Strain rate effect on structural steel under cyclic loading. *Journal of Engineering Mechanics* 1987; **113**(9):1292–1301.
9. Lee GC, Chang K-C, Sugiura K. The experimental basis of material constitutive laws of structural steel under cyclic and nonproportional loading. *Stability and Ductility of Steel Structures Under Cyclic Loading*. CRC Press, 1991. p 3–14.
10. Yamada S, Yamaguchi M, Takeuchi T, Wada A. *Hysteresis Model of Steel Material for the Buckling Restrained Brace Considering the Strain Rate Dependency, in Proceedings of 13th World Conference on Earthquake Engineering*. Vancouver: B.C., Canada, 2004.
11. Yu Y-J, Tsai K-C, Li C-H, Weng Y-T, Tsai C-Y. Earthquake response analyses of a full-scale five-story steel frame equipped with two types of dampers. *Earthquake Engineering and Structural Dynamics* 2013; **42**(9):1301–1320.
12. J. T. Lanning, Using buckling-restrained braces on long-span bridges near seismic faults, Ph.D Dissertation, University of California, San Diego, 2014.
13. Fahnestock LA, Sause R, Ricles JM, Lu L-W. Ductility demands on buckling-restrained braced frames under earthquake loading. *Earthquake Engineering and Engineering Vibration* 2003; **2**(2):255–268.
14. L. A. Fahnestock, R. Sause and J. M. Ricles, Analytical and large-scale experimental studies of earthquake-resistant buckling-restrained braced frame systems, ATLSS Report No. 06-01, Engineering Research Center for Advanced Technology for Large Structural Systems, Lehigh University, Bethlehem, PA, 2006.
15. Zona A, Dall'Asta A. Elastoplastic model for steel buckling-restrained braces. *Journal of Constructional Steel Research* 2012; **68**(1):118–125.
16. Gu Q, Zona A, Penga Y, Dall'Asta A. Effect of buckling-restrained brace model parameters on seismic structural response. *Journal of Constructional Steel Research* 2014; **98**:100–113.
17. Rossi P. Importance of isotropic hardening in the modeling of buckling restrained braces. *Journal of Structural Engineering* 2015; **141**(4):1–11.
18. Zsarnóczay Á, Budaházy V, Vigh LG, Dunai L. Cyclic hardening criteria in EN 15129 for steel dissipative braces. *Journal of Constructional Steel Research* 2013; **83**:1–9.
19. Karavasilis TL, Kerawala S, Hale E. Hysteretic model for steel energy dissipation devices and evaluation of a minimal-damage seismic design approach for steel buildings. *Journal of Contructional Steel Research* 2011; **70**:358–367.
20. J. Chaboche, K. Dang Van and G. Cordier, Modelization of the strain memory effect on the cyclic hardening of 316 stainless steel, in *Procceding of 5th International Conference on Structural Mechanics in Reactor Technology*, *Division L11/3*, Berlin, 1979.
21. Dafalias YF. Bounding surface plasticity model for steel under cyclic loading. *Stability and Ductility of Steel Structures Under Cyclic Loading*. CRC Press, 1991. p 25–36.
22. Menegotto M, Pinto PE. Method of analysis for cyclically loaded R.C. plane frames including changes in geometry and non-elastic behavior of elements under combined normal force and bending. *Method of analysis for cyclically loaded R.C. plane frames including changes in geometry and non-elastic behavior of elements under combined normal force and bending*. : Lisbon, 1973.
23. F. Filippou, E. Popov and V. Bertero, Effects of bond deterioration on hysteretic behavior of reinforced concrete joints, Report No. UCB/EERC-83/19,University of California, Berkeley, Berkeley, 1983.
24. F. Filippou, OpenSees—Open System for Earthquake Engineering Simulation: Steel02.cpp, 16 September 2010. [Online].Available:http://opensees.berkeley.edu/WebSVN/filedetails.php?repname=OpenSees&path=%2Ftrunk%2FSRC%2Fmaterial%2Funiaxial%2FSteel02.cpp. [Accessed 2015].
25. B. Saxey and M. Daniels, Characterization of overstrength factors for buckling restrained braces, in *Proceedings in Australian Structural Engineering Conference 2014*, Auckland, NZ, 2014.
26. Dodd LL, Restrepo-Posada JI. Model for predicting cyclic behavior of reinforcing steel. *Journal of Structural Engineering* 1995; **121**(3):433–445.
27. F. McKenna, G. L. Fenves and M. H. Scott, Open System for Earthquake Engineering Simulation, *Pacific Earthquake Engineering Research Center*, 2000.
28. A. Schellenberg, OpenSEES: ElasticMultiLinear Material, [Online]. Available: http://opensees.berkeley.edu/wiki/index.php/ElasticMultiLinear_Material. n.d
29. FEMA P695, Quantification of building seismic performance factors, Federal Emergency Management, Washington, DC, 2009.
30. Baker JW. Conditional mean spectrum: tool for ground motion selection. *Journal of Structural Engineering* 2011; **137**(3):322–331.
31. ASCE, ASCE Standard ASCE/SEI7 - 10: minimum design loads for buildings and other structures, Reston, Virginia: American Society of Civil Engineers, 2010.


Copyright © 2016 John Wiley & Sons, Ltd.

DOI: 10.1002/eqe